Biochemistry **2001,** *40,* 375−386

Solution Structure and Dynamic Character of the Histidine-Containing Phosphotransfer Domain of Anaerobic Sensor Kinase ArcB from *Escherichia coli*[†,‡]

Takahisa Ikegami,[§] Terumasa Okada,[§] Izuru Ohki,[§] Junya Hirayama,[§] Takeshi Mizuno,[||] and Masahiro Shirakawa*[,§]

Graduate School of Biological Sciences, Nara Institute of Science and Technology, 8916-5 Takayama, Ikoma, Nara 630-0101, Japan, and Laboratory of Molecular Microbiology, School of Agriculture, Nagoya University, Chikusa-ku, Nagoya 464-8601, Japan

Received July 12, 2000; Revised Manuscript Received September 25, 2000

ABSTRACT: An *Escherichia coli* sensor kinase, ArcB, transfers a phosphoryl group to a partner response regulator in response to anaerobic conditions. Multidimensional NMR techniques were applied to determine the solution structure of the histidine-containing phosphotransfer signaling domain of ArcB ($\mathrm{HPt_{ArcB}}$), which has a phosphorylation site, His717. The backbone dynamics were also investigated by analyses of the ^{15}N relaxation data and amide hydrogen exchange rates. Furthermore, the protonation states of the histidine imidazole rings were characterized by means of ^{1}H and ^{15}N chemical shifts at various pHs. The determined solution structure of $\mathrm{HPt_{ArcB}}$ contains five helices and forms a four-helix bundle motif like other HPt domains. The obtained order parameters, S^2, $\{^1\mathrm{H}\}-^{15}\mathrm{N}$ heteronuclear NOE values, and chemical exchange parameters, R_{ex}, showed that the α-helical regions of $\mathrm{HPt_{ArcB}}$ are rigid on both picosecond to nanosecond and microsecond to millisecond time scales. On the other hand, helix D, which contains His717, exhibited low protection factors of less than 4000, indicating the presence of fluctuations on a slower time scale in helix D. These results suggest that $\mathrm{HPt_{ArcB}}$ may undergo a small conformational change in helix D upon phosphorylation. It was also shown that the imidazole ring of His717 has a pK_a value of 6.76, which is similar to that of a solvent-exposed histidine imidazole ring, and that a pair of deprotonated neutral tautomers are rapidly exchanged with each other. This is consistent with the solution structure of $\mathrm{HPt_{ArcB}}$, in which the imidazole ring of His717 is exposed to the solvent.

Bacteria respond to various changes of the environment, such as osmotic stress, anaerobic conditions, and chemical concentrations, through intracellular signal transduction systems. The mechanism most widely used is phosphotransfer signaling, in which protein phosphorylation and dephosphorylation events take place sequentially to transmit the signals from the environment to regulatory systems involving transcription factors (*1*). The mechanisms for bacterial phosphotransfer signaling are collectively referred to as "two-component regulatory systems", which are composed of "sensor kinase" and "response regulator" proteins (*2*). In a typical two-component system, a signal captured by the receptor domain of a sensor kinase is transferred to the receiver domain of the corresponding response regulator through the relaying of a phosphoryl group from a histidine residue in the histidine−kinase (transmitter) domain of the sensor kinase to an aspartate residue in the receiver domain of the response regulator (His-to-Asp phosphorelay). Recently, two-component systems have also been found in archaea and eukarya, including yeast, fungi, and plants (*3*).

An *Escherichia coli* sensor kinase, ArcB, phosphorylates the partner response regulator, ArcA, in response to anaerobic conditions (*4*). ArcB is a hybrid sensor kinase containing multiple phosphorylation domains: a histidine-containing phosphotransfer (HPt)[1] signaling domain and a receiver domain in addition to the receptor and histidine−kinase (transmitter) domains, which are the two domains constituting a typical sensor kinase (*5*). Recent in vitro studies have yielded a scheme for the phosphorelaying in the multistep signal transduction from ArcB to ArcA (*4*). First, a phosphoryl group is transferred from His292 in the histidine−kinase domain to Asp576 in the receiver domain and subsequently to His717 in the HPt domain (*4*). This phosphotransfer occurs within a molecule. Finally, Asp54 of ArcA receives the phosphoryl group from the HPt domain of ArcB. The phosphorylated ArcA modulates the expression of the genes related to the respiratory systems. Interestingly, the budding yeast *Saccharomyces cerevisiae* utilizes a similar mechanism for osmoresponsive signal transduction, and the component that corresponds to the HPt domain, Ypd1p (YPD1), exists independently of the other components as a protein (*6*, *7*). Thus, in addition to unidirectional signal

---

[†] This work was supported through grants to M.S. and T.I. from the Ministry of Education, Science and Culture of Japan.

[‡] The atomic coordinates have been deposited in the Protein Data Bank, accession code 1FR0.

* To whom correspondence should be addressed. E-mail: shira@bs.aist-nara.ac.jp. Fax: +81-743-72-5579. Phone: +81-743-72-5571.

[§] Nara Institute of Science and Technology.

[||] Nagoya University.

[1] Abbreviations: HMBC, heteronuclear multiple-bond correlation; HMQC, heteronuclear multiple-quantum correlation; HPt, histidine-containing phosphotransfer; HSQC, heteronuclear single-quantum correlation; NMR, nuclear magnetic resonance; NOE, nuclear Overhauser effect; NOESY, NOE spectroscopy; TOCSY, total correlation spectroscopy.

10.1021/bi001619g CCC: $20.00

transduction, the HPt domains may mediate signal-branching events, such as cross-talk, integration of multisignals, signal feedback, adaptation, and modulation through phosphatases, in the multiple His-to-Asp phosphorelay signaling mechanisms (*1*).

Recently, the crystal structure of the HPt domain (Thr654–Lys778, 125 amino acid residues) of *E. coli* ArcB (HPt_{ArcB}) was solved at 1.57 Å resolution (PDB code, 2A0B) (*8*, *9*). Furthermore, the crystal or solution structures of the following HPt domains have been determined: Ypd1p from *S. cerevisiae* (*6*, *7*), P1 domain of CheA from *E. coli* (*10*), and dimeric Spo0B from *Bacillus subtilis* (*11*). All these structures commonly have a four-helix bundle motif and a histidine residue as the phosphorylation site at a similar position. However, little is known about the dynamic properties of these HPt domains (proteins) or about the character of the histidine residue directly involved in the phosphotransfer, except for the results of nuclear magnetic resonance (NMR) analyses of the phosphotransfer domain of CheA (*10*, *12*). Here, we report the structure of HPt_{ArcB} determined by NMR, the backbone dynamics based on the ^{15}N relaxation data and on the rates of the amide hydrogen exchange with the solvent, and the characters of the histidine residues based on the results of pH titration of their imidazole rings.

EXPERIMENTAL PROCEDURES

Sample Preparation. For NMR experiments, uniformly ^{15}N- or ^{15}N-,^{13}C-labeled HPt_{ArcB} was produced by growing *Escherichia coli* K-12 strain DZ225, carrying plasmid pSU2DH, which contains the gene of HPt_{ArcB}, in M9 minimal medium containing 0.5 g/L $^{15}NH_4Cl$, without or with 1.0 g/L [*U*-^{13}C]-D-glucose, respectively. The expressed proteins were purified by DEAE-Sepharose (Pharmacia) and Mono-Q (Pharmacia) ion-exchange and Sephacryl S-100 (Pharmacia) gel-filtration chromatographies as described (*8*). Samples for NMR measurements typically comprised 1.5 mM HPt_{ArcB}, 50 mM KH_2PO_4–K_2HPO_4 (pH 6.5 at 37 °C), 50 mM KCl, and 1 mM dithiothreitol (DTT) in 90% H_2O/10% ^2H_2O or 99.8% ^2H_2O.

NMR Spectroscopy. Most NMR spectra were acquired at 310 K with a Bruker DMX500 or DRX500 spectrometer equipped with a triple resonance (^1H, ^{15}N, and ^{13}C) probe with self-shielded triple-axis gradient coils. The ^1H, ^{15}N, and ^{13}C resonances of the backbone were assigned using a combination of multidimensional and multiresonance spectra: 3D HNCO, HN(CA)CO, CBCA(CO)NH, CBCANH, HNCA, HN(CA)HA, HBHA(CBCACO)NH, and HBHA-(CBCA)NH (*13*). The resonances of the side chains were assigned using 2D TOCSY, 3D H(CCO)NH, (H)C(CO)NH, HCCH-TOCSY, and ^{15}N-edited TOCSY spectra (*13*). In particular, the resonances of the aromatic side chains were assigned using 2D TOCSY, (HB)CB(CGCD)HD, and (HB)-CB(CGCDCE)HE spectra (*14*). The methyl groups of the leucine and valine residues were stereospecifically assigned by means of constant-time (28 ms) and $^1J_{CC}$-resolved ^1H–^{13}C heteronuclear single-quantum correlation (HSQC) experiments using 15% fractionally ^{13}C-labeled HPt_{ArcB} dissolved in 99.8% ^2H_2O (*15*). For interproton distance constraints, 2D NOESY, 3D ^{15}N-edited NOESY, ^{13}C-edited NOESY, and 4D ^{13}C, ^{13}C-edited NOESY spectra were acquired with the mixing time of 100 ms (*13*). For dihedral angle constraints, a 2D $^3J_{HNH\alpha}$-resolved ^1H–^{15}N heteronuclear multiple-quantum correlation (HMQC-J) spectrum was acquired (*13*). Most experiments in which amide protons were directly detected included the combination of the sensitivity-enhancement and gradient-echo methods for the indirect ^{15}N dimensions (*13*). The other indirect dimensions were recorded in the States-TPPI manner (*16*). Samples dissolved in 90% H_2O/10% ^2H_2O were used for the experiments for detecting amide protons directly, and samples dissolved in 99.8% ^2H_2O were used for the other experiments. The NMR data were processed and analyzed using the NMRPipe version 1.7 (*17*) and Pipp version 4.2.4 (*18*) software packages, respectively.

Structure Calculation. The NOE-based constraints derived from strong, medium, and weak cross-peaks were categorized and assumed to correspond to the upper limits for interproton distances of 3.0, 4.0, and 5.0 Å, respectively (*19*). Pseudoatom corrections were applied to the upper bound constraints involving methyl, methylene, and aromatic ring protons as described (*19*). The NOE list was not filtered for removal of constraints of no structural value. The distance constraints for hydrogen bonds applied for slowly exchanging amides were 2.8–3.3 Å for N–O pairs and 1.8–2.3 Å for H–O pairs. A pair of these constraints was applied to each hydrogen bond to restrict both the length and angle of the bond. The hydrogen bond constraints in α-helices were estimated on the basis of the short- and medium-range NOE patterns that are typical of α-helices (*19*). The backbone torsion angles, ϕ, were estimated from the scalar $^3J_{HNH\alpha}$ coupling constants derived from the 2D HMQC-J spectrum. The angle constraints used were $-60 \pm 20°$ for $^3J_{HNH\alpha} < 2.0$ Hz, $-60 \pm 40°$ for $^3J_{HNH\alpha} > 2.0$ and <4.0 Hz, and $-120 \pm 40°$ for $^3J_{HNH\alpha} > 8.0$ Hz.

At the stage of structural constraint collection, program DYANA version 1.5 (molecular dynamics in a torsion angle space with 25 000 steps) was used (*20*). Finally, an ensemble of 100 structures of HPt_{ArcB} was calculated with program X-PLOR version 3.851 (*21*). The standard simulated annealing protocol (sa.inp file) with 24 000 steps at a high temperature (1000 K) and 12 000 steps for the cooling process was used. The 30 best structures were analyzed with the MOLMOL (*22*) and AQUA-PROCHECK-NMR (*23*) software packages. The secondary structure elements were determined on the basis of the results of AQUA-PROCHECK-NMR analysis (*23*).

Measurement of ^{15}N R_1, R_2, and NOE. Spectra for ^{15}N longitudinal relaxation rates, R_1, ^{15}N transverse relaxation rates, R_2, and {^1H}–^{15}N steady-state heteronuclear NOE values were acquired at 310 K with a Bruker DRX500 spectrometer operated at the ^{15}N frequency of 50.7 MHz (^1H frequency, 500.23 MHz). The pulse sequences including the combination of the sensitivity-enhancement and gradient-echo methods for the indirect ^{15}N dimensions were used in these experiments (*24*). R_1 relaxation was measured with delays of 5, 65, 145, 245, 365, 525, 755, and 1145 ms and R_2 relaxation with delays of 14.4, 28.8, 43.2, 57.6, 72.0, 100.8, and 144.0 ms. The delay between ^{15}N 180° pulses in the Carr–Purcell–Meiboom–Gill (CPMG) sequence for the R_2 measurements was 900 μs. In the heteronuclear NOE experiment, a relaxation delay of 3.0 s before ^1H saturation for 3.0 s was applied for the NOE enhancement spectrum, while a relaxation delay of 6.0 s without ^{1}H saturation was applied for the reference spectrum. The ^{1}H saturation was achieved with 120° ^{1}H pulses applied every 5 ms. The numbers of complex points and spectral widths were 200 and 1013.7 Hz and 512 and 7002.8 Hz for the ^{15}N and ^{1}H dimensions, respectively. The ^{1}H carrier was set to the frequency of the water resonance (4.7 ppm), and the ^{15}N carrier was set to 119.8 ppm. For the R_1, R_2, and NOE measurements, 32, 32, and 64 scans were accumulated, respectively. All data sets were processed with the program NMRPipe (*17*). Lorentz-to-Gauss transformations were applied to both ^{1}H and ^{15}N dimensions prior to the respective Fourier transformations.

Estimation of ^{15}N R_1, R_2, and NOE. A series of peak heights at the fixed amide resonance position for each residue was collected from all the spectra. The root-mean-square (rms) deviations of the background noise were used as the uncertainties of the measured intensities in the NOE experiment. The uncertainties for the R_1 and R_2 experiments were estimated from the pairwise rms differences of duplicate spectra, which were obtained with the shortest relaxation delays under the same conditions. Each R_1 and R_2 value was determined by fitting a series of measured intensities to a two-parameter function, $I(t) = I_0 \exp(-R_{1,2}t)$, where $I(t)$ is the intensity after time delay t, and I_0 is the intensity at time zero. Nonlinear least-squares fitting according to the Levenberg−Marquardt method (*25*) was employed for optimization of the values of the I_0 and $R_{1,2}$ parameters using the program CURVEFIT (*26*). Only results with χ^2 values smaller than the simulated ones at the 95% confidence level were used. Here, χ^2 equals $\sum\{I_c(t) - I_e(t)\}^2/\sigma_I^2$ ($I_c(t)$, the intensity calculated from the fitting parameters; $I_e(t)$, the experimental intensity; σ_I, the uncertainty of the experimental value), and summation was performed for the available experimental data set. The uncertainties of the R_1 and R_2 values were estimated by Monte-Carlo simulations. The $\{^1\text{H}\}-^{15}\text{N}$ steady-state NOE values were determined from the ratios of the peak intensities with and without proton saturation ($I_{\text{NOE}}/I_{\text{NON-NOE}}$). The uncertainties of the NOE values were estimated according to the error propagation equation (*25*).

Model-Free Analysis. An initial estimate of the overall rotational correlation time, τ_m, was obtained from the mean of the R_2/R_1 ratios that were limited to within one standard deviation (SD) (*24*). In the model-free analysis developed by Lipari and Szabo (*27*), with an assumed isotropic rotational diffusion model, the following five dynamic models were applied according to Mandel et al. (*26*). The models and the combinations of optimized internal motion parameters were (M1) S^2, (M2) S^2 and τ_{ef}, (M3) S^2 and R_{ex}, (M4) S^2, τ_{ef}, and R_{ex}, and (M5) S_f^2, S^2, and τ_{es} where S^2 is the square of the order parameter, which represents the degree of spatial restriction of the internal motion, τ_e is the effective correlation time of the internal motion, R_{ex} is the chemical exchange rate, and subscripts f and s represent fast and slow time scales, respectively. The data were fitted to each of the five dynamic models with τ_m fixed at the initially estimated value, and one of the dynamic models was statistically selected for each backbone amide ^{15}N spin by means of Monte-Carlo simulations and *F*-statistical tests as described (*26*). Then, τ_m and the internal motion parameters were simultaneously optimized with the selected dynamic models. The uncertainty for each parameter was estimated by means of Monte-Carlo simulations. All analyses were performed using program MODELFREE-4.10 (*26*).

Model-free analysis with an assumed anisotropic rotational diffusion model was performed as follows. First, the R_2/R_1 ratios for the residues that had significant internal motions manifested by $\{^1\text{H}\}-^{15}\text{N}$ steady-state NOE values of less than 0.65 were excluded. Then, the R_2/R_1 ratios for the residues that were assumed to undergo chemical exchange by satisfying the inequality, $\{(\langle T_2\rangle - T_2)/\langle T_2\rangle - (\langle T_1\rangle - T_1)/\langle T_1\rangle\} > 1.5$ SD, were also excluded, where T_n is the reciprocal of R_n, $\langle T_n\rangle$ is the average T_n value, and SD is the standard deviation of the left-hand side of the inequality (*28*). The magnitude and orientation of the axially symmetric rotational diffusion tensor, *D*, were initially estimated from the remaining R_2/R_1 ratios and the molecular coordinates of HPt$_{\text{ArcB}}$ (*9*) with program R2_R1_DIFFUSION in the MODELFREE-4.10 package (*26*). On the basis of the estimated *D* tensor, model-free analysis with the axially symmetric anisotropic diffusion model was performed. The procedure was the same as that employed for the isotropic diffusion model except that the diffusion tensor, *D*, and the molecular coordinates were used instead of the single overall rotational correlation time, τ_m.

Hydrogen Exchange Experiments. Samples of ^{15}N-labeled HPt$_{\text{ArcB}}$ dissolved in 50 mM phosphate buffer, pH 5.5 and 6.5, containing 50 mM KCl and 1 mM DTT were lyophilized, dissolved in ^{2}H$_2$O, and immediately applied to a Bruker DRX800 spectrometer, which had been previously tuned and set at 310 K. A series of HSQC spectra were acquired every 15−60 min at 50 points within 2118 min after dissolution (pH 5.5) and at 33 points within 1093 min (pH 6.5). The ^{15}N and ^{1}H dimensions were recorded with 64 and 1024 complex points with spectral widths of 1622 Hz centered at 119.4 ppm and 13 021 Hz centered at 4.70 ppm, respectively. The combination of the sensitivity-enhancement and gradient-echo methods was used for the indirect ^{15}N dimension (*13*). Linear prediction and Lorentz-to-Gauss transformation were applied to ^{15}N and ^{1}H dimensions, respectively. Each spectrum was processed identically. The $^1\text{H}-^{15}\text{N}$ cross-peaks in the first spectrum were picked with Pipp software (*18*), and a series of peak heights at the fixed resonance position for each residue was collected from all the spectra. Amide proton exchange rates, k_{ex}, were determined by fitting a series of peak heights to the exponential function, $I(t) = I_0 \exp(-k_{ex}t) + C$, where $I(t)$ and I_0 are the peak heights after time delay t and at time zero, respectively, and C is the correction for a baseline offset. The uncertainties of the k_{ex} values were estimated by Monte-Carlo simulations with the rms deviations of the spectral noise. Protection factors, P, were calculated with the equation, $P = k_{rc}/k_{ex}$, where k_{rc} denotes the amide proton exchange rate in a random chain conformation (*29*). The k_{rc} values were calculated according to the method of Bai et al. taking the primary sequence, temperature, and difference between the pH and pD into account (*29*). The free-energy for local transient unfolding, ΔG, was obtained according to the equation, $\Delta G = RT \ln P$, where R is the Boltzman constant.

pH Titration of Histidine Residues. Heteronuclear multiple bond $^1\text{H}-^{15}\text{N}$ correlation (HMBC) experiments were performed with a DMX500 spectrometer as described (*30*). The samples used typically comprised 0.5−0.7 mM ^{15}N-labeled

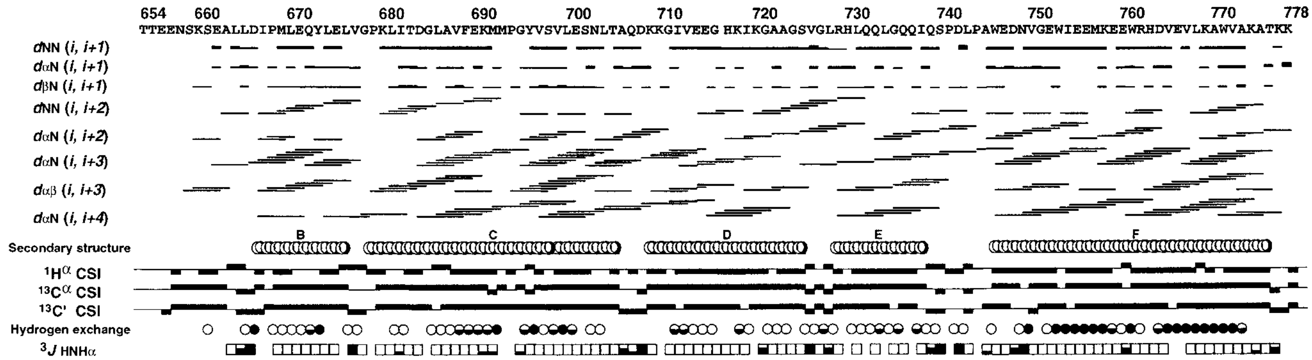

FIGURE 1: The structure information obtained in the NMR experiments. Summary of the sequential and medium-range NOE connectivities, secondary structure, chemical shift indices, amide hydrogen exchange rates, and $^3J_{\mathrm{HNH}\alpha}$ coupling constants for HPt$_{\mathrm{ArcB}}$. The NOE connectivities are represented by bars, the size of which indicates the NOE intensity (strong, medium, or weak). The notation $d_{\alpha\mathrm{N}(i,i+1)}$, for example, represents the connectivity between the α proton resonance of a residue (*i*) and the amide proton resonance of the subsequent residue ($i + 1$) in the sequence. Amide protons that were exchanged with the solvent slowly at pH 6.5 and 310 K are indicated. Residues with exchange rates of >0.07 min^{-1} are indicated by open circles, ones of >0.02 and <0.07 min^{-1} by half-closed circles, and ones of <0.02 min^{-1} by closed circles. The three-bond scalar coupling constants between spins ^{1}H$^{\mathrm{N}}$- and ^{1}H$^\alpha$($^3J_{\mathrm{HNH}\alpha}$) < 3.0 Hz are indicated by open boxes, >3.0 and <5.0 Hz by one-third closed boxes, >5.0 and <8.0 Hz by two-thirds closed boxes, and >8.0 Hz by closed boxes. The chemical shift indices (CSI) (*31*) are plotted for ^{1}H$^\alpha$, ^{13}C$^\alpha$, and ^{13}C′ resonances. The upper bars represent +1; lower bars, −1; and horizontal lines, 0. The figure was produced with the programs VINCE (1996, Rowland Institute for Science) and DYANA (*20*).

HPt$_{\mathrm{ArcB}}$, 50 mM KH_2PO_4−K_2HPO_4, 50 mM KCl, 1 mM DTT, and 10% ^2H_2O. For measurements at pHs higher than 8.5, 50 mM Tris-HCl buffer was used instead of the phosphate buffer. Small aliquots of 1 N NaOH or HCl were added to adjust the pH value at 0.2−0.3 intervals. For suppression of the ^1J-coupled ^{1}H−^{15}N coherence in the imidazole ring of a histidine residue, a ^{15}N 90° pulse was applied after ^{1}H evolution for 5.56 ms. A second ^{15}N 90° pulse was applied after ^{1}H evolution for 65.56 ms for the coherence transfer from the carbon-attached protons to the ^2J- or ^3J-coupled nitrogens. The ^{15}N dimension was recorded in the States-TPPI manner (*16*). Data sets were typically acquired with 400 and 1024 complex points with spectral widths of 5100 Hz (100.7 ppm) centered at 200.3 ppm and 6010 Hz centered at 4.7 ppm for the ^{15}N and ^{1}H dimensions, respectively. After Fourier transformation of both dimensions, spectra were phased in the ^{15}N dimension and then calculated in the absolute-value mode in the ^{1}H dimension. The ^{1}H and ^{15}N chemical shifts obtained at various pHs between 3.69 and 9.41 were fitted by means of a nonlinear optimization procedure to the Henderson−Hasselbalch equation, $\delta_{\mathrm{obs}} = [\delta_{\mathrm{xh}} + \delta_{\mathrm{x}}10^{(\mathrm{pH}-\mathrm{p}K_{\mathrm{a}})}]/[1 + 10^{(\mathrm{pH}-\mathrm{p}K_{\mathrm{a}})}]$, where δ_{obs} is the observed chemical shift, and δ_{xh} and δ_{x} are the chemical shifts for protonated and deprotonated imidazole rings, respectively.

RESULTS

Resonance Assignments. The ^{1}H, ^{15}N, and ^{13}C chemical shifts were assigned by means of the multidimensional and multiresonance NMR methods using ^{15}N- or ^{15}N-,^{13}C-labeled HPt$_{\mathrm{ArcB}}$. The main chain was assigned unambiguously by taking advantage of the well-resolved carbonyl ^{13}C(^{13}C′) chemical shifts in the combination of 3D HNCO and HN(CA)CO spectra. This advantage is particularly great for helix-rich proteins such as HPt$_{\mathrm{ArcB}}$, whose ^{1}H$^\alpha$ and ^{13}C$^\alpha$ resonances tend to be confined to narrow frequency ranges. Well-resolved ^{13}C$^\beta$ chemical shifts were also useful for main chain assignment by means of the combination of 3D CBCA(CO)NH and CBCANH spectra. The resonance assignments for the backbone amide ^{1}H and ^{15}N nuclei were completed except for those of the N-terminal two residues and the sixth one (Thr654, Thr655, and Ser659). The ^{1}H−^{15}N amide signals of these residues were not observed in ^{1}H−^{15}N HSQC spectra, probably due to conformational averaging or rapid amide hydrogen exchange with the solvent. For the side chains, 93% and 90% of the expected ^{1}H and ^{13}C resonances were assigned, respectively. All the methyl groups of the 14 leucine and 10 valine residues were assigned stereospecifically by using 15% fractionally ^{13}C-labeled HPt$_{\mathrm{ArcB}}$ (*15*). Figure 1 shows the sequential and medium-range NOE connectivities, amide proton exchange rates, $^3J_{\mathrm{HNH}\alpha}$ coupling constants, and chemical shift indices (CSI) for ^{13}C$^\alpha$, ^{1}H$^\alpha$, and ^{13}C′ resonances (*31*). The α-helical regions were characterized by NOE cross-peaks between the α proton of residue *i* and the amide proton of residue $i + 3$ ($d_{\alpha\mathrm{N}(i,i+3)}$) or $i + 4$ ($d_{\alpha\mathrm{N}(i,i+4)}$). The locations of the α-helices were also indicated by characteristic deviations of the ^{1}H$^\alpha$, ^{13}C$^\alpha$, and ^{13}C′ chemical shift values from those for random coils with CSI of −1, +1, and +1, respectively (*31*), slow rates of exchange of the amide protons with solvent deuterons due mainly to the formation of the relevant hydrogen bonds, and small $^3J_{\mathrm{HNH}\alpha}$ coupling constants (<4 Hz).

Structure Calculations. The three-dimensional structure of HPt$_{\mathrm{ArcB}}$ was calculated by means of the X-PLOR simulated annealing standard protocol on the basis of 1188 nuclear Overhauser effect (NOE)-derived interproton distance constraints, 83 ϕ dihedral angle constraints, and 77 hydrogen bond constraints. Degeneracy of the aliphatic proton resonances often made it difficult to assign long-range NOE cross-peaks in the 3D ^{13}C-edited NOESY spectrum. The ambiguity in these assignments was effectively eliminated by using the 4D ^{13}C,^{13}C-edited NOESY spectrum, from which 156 long-range ($|i - j| > 4$) NOE-based constraints were collected.

A total of 100 structures were calculated. Of these, 30 final structures, which showed the lowest energy values, no distance constraint violation of >0.5 Å, and no dihedral angle constraint violation of >5°, were selected. Superpositioning of these 30 structures is shown in Figure 2a, and the constraints used and the structural statistics for the final

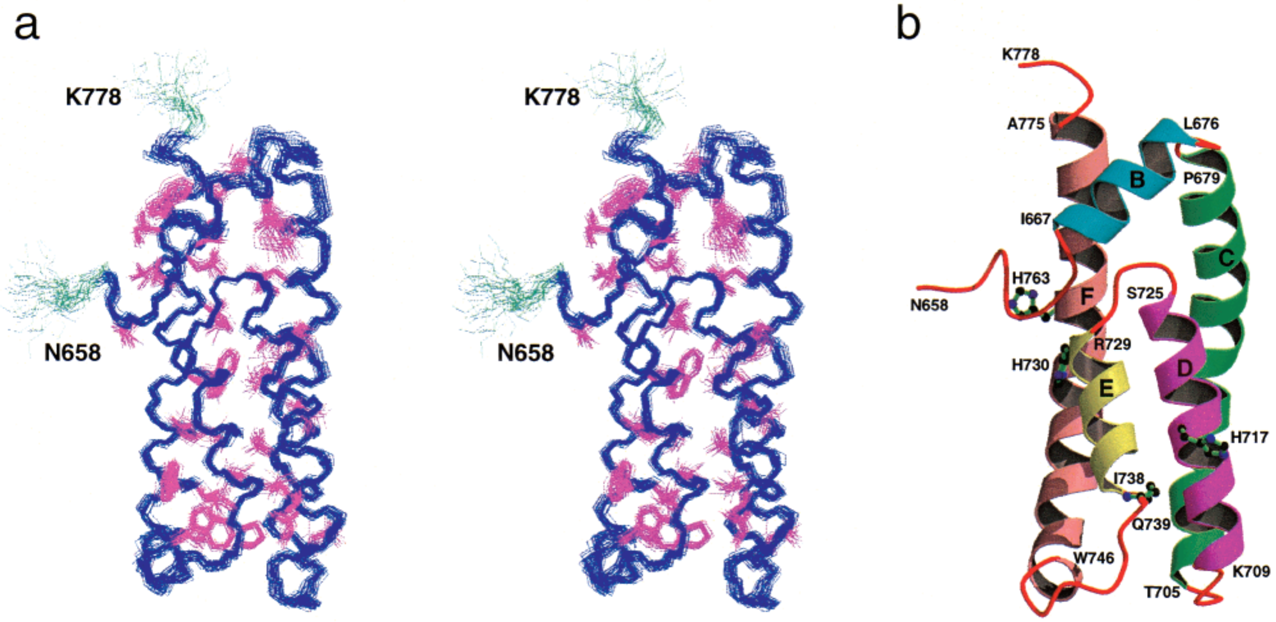

FIGURE 2: Tertiary structures of HPt_{ArcB}. (a) A stereoview of the best-fit superpositioning of the final 30 structures, which were calculated by means of the simulated annealing procedure of X-PLOR 3.851 (*21*). The backbone heavy atoms (N, C^{α}, and C′) of the regions colored blue (Glu662−Ala775) are superimposed. The disordered N-terminal four residues are not included for clarity. The side chains of the noncharged and buried residues, whose solvent accessibility values are less than 20%, are also shown in magenta. (b) Schematic ribbon drawing of the representative solution structure. The secondary structure elements and both end residues of each α-helix are shown. The side chains of the three histidine residues (His717, His730, and His763) and Gln739 are also shown as a ball-and-stick model. The figure was drawn with the programs MOLSCRIPT (*52*) and RASTER3D (*53*). The direction of the molecule in (a) is almost the same as in (b).

Table 1: Structural Statistics[a] for HPt_{ArcB}

total number of distance constraints	1265
intraresidual	178
sequential ($\|i - j\| = 1$)	316
medium range ($\|i - j\| \leq 4$)	413
long range ($\|i - j\| > 4$)	281
hydrogen bonds	77
number of dihedral angle constraints	83
maximum violation of distance constraints	0.13 Å
maximum violation of dihedral angle constraints	1.3°
maximum violation of van der Waals distances	0.34 Å
rms deviations from experimental constraints	
distance	0.0086 ± 0.0006 Å
angle	0.113 ± 0.037°
rms deviations from idealized covalent geometry	
bonds	$0.0014 \pm 3.55 \times 10^{-5}$ Å
angles	0.486 ± 0.002°
impropers	0.357 ± 0.002°
X-PLOR potential energy (E_{total})	167.7 ± 1.91
PROCHECK Ramachandran plot statistics (residues Glu662−Ala775)	
residues in most favored regions	88.7%
residues in additional allowed regions	10.2%
residues in generously allowed regions	1.1%
residues in disallowed regions	0.0%
rms deviations from mean coordinate positions (residues Glu662−Ala775)	
backbone heavy atoms	0.452 Å
all heavy atoms	0.927 Å

[a] These statistics comprise the ensemble of the final 30 simulated annealing structures (Thr654−Lys778) calculated with X-PLOR 3.851 (*21*). All variances quoted are ±1 SD.

structures are summarized in Table 1. The rms deviations of these structures from the average structure were 0.452 Å for the backbone heavy atoms in the whole sequence excluding the amino (N)-terminal eight residues and carboxy (C)-terminal three residues (Glu662−Ala775) and 0.927 Å for all heavy atoms in the same region. The structures in this nonterminal region exhibited good geometry, with no residue in disallowed regions of a Ramachandran plot (*23*). X-PLOR and DYANA (*20*) provided almost the same structures. The average DYANA target function value of the best 30 structures that were selected out of the 100 calculated ones was 0.79 ± 0.10 (1 SD). The rms deviations of the total 60 structures that were calculated with X-PLOR or DYANA were 0.511 Å for the backbone heavy atoms and 0.965 Å for all heavy atoms in the same region as described above.

Structure Description. As displayed in Figure 2a, the backbone of residues Glu662−Ala775 and hydrophobic side chains have been well defined. In contrast, the N-terminal eight residues have not been well-defined owing to the small number of medium- and long-range NOEs (Figure 1). The X-ray study of HPt_{ArcB} at 1.57 Å resolution by Kato et al. (*9*) also showed that the electron density of the N-terminal five residues (Thr654−Asn658) and C-terminal two residues (Lys777 and Lys778) was missing and that the temperature factors, which represent the dynamic disorder due to the temperature-dependent vibration of the atoms in a crystal, for the subsequent N-terminal five residues (Ser659−Ala663) were more than 30 $Å^2$. The solution structure determined in this experiment and the crystal structure are almost the same. The mean and distribution of the pairwise rms deviations between the crystal structure and each of the 30 solution structures were 1.29 ± 0.07 Å (1 SD) for backbone heavy atoms of residues Glu662−Ala775.

HPt_{ArcB} has a kidney-shaped and all-α structure consisting of five helices (B−F) (Figure 2b). In the crystal structure (*9*), residues Lys660−Leu664 have been assigned to helix A, but this region does not adopt a helical conformation in the solution structure. This region protrudes and is flexible, as indicated by the small heteronuclear $\{^{1}H\}-^{15}N$ NOE values (<0.51). The locations of the other helices (B−F) in the solution structure are the same as those in the crystal

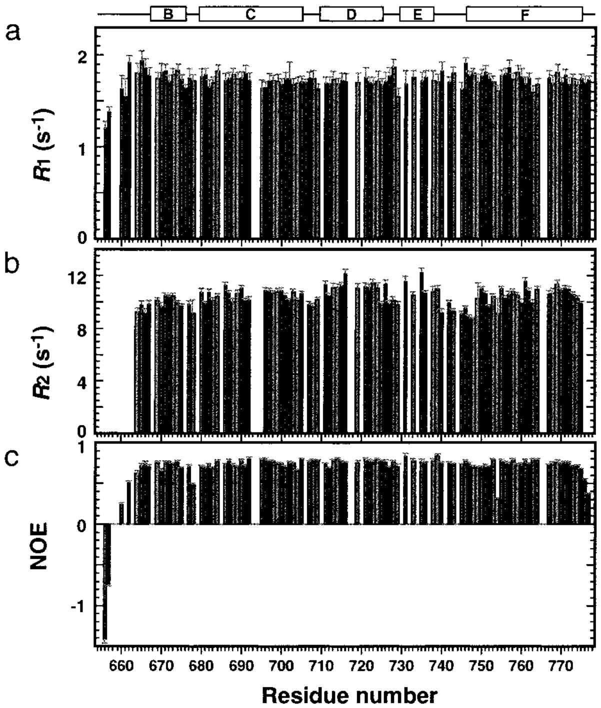

FIGURE 3: Plots of amide ^{15}N R_1, R_2, and NOE against residue numbers. The data were measured at the ^{15}N frequency of 50.7 MHz, which corresponds to a ^{1}H frequency of 500.23 MHz: (a) longitudinal relaxation rates, R_1; (b) transverse relaxation rates, R_2; (c) heteronuclear {^{1}H}−^{15}N steady-state NOE values defined as $I_{NOE}/I_{NON-NOE}$, where I_{NOE} and $I_{NON-NOE}$ are the peak intensities with and without ^{1}H saturation, respectively. For plots a−c, the error bars indicate 1 SD values of the uncertainties of the data. The secondary structure is indicated at the top.

structure. Helices C−F are arranged in an up-and-down topology, forming a four-helix bundle motif. The remaining helix, B, lies on long helices C and F and covers the loop between short helices D and E. Helices C and F bend around the center of each helix. The phosphorylation site, His717, is located in the center of helix D, and its imidazole ring is exposed to the solvent.

^{15}N Relaxation Data. To characterize the dynamic properties of HPt$_{ArcB}$, we determined ^{15}N longitudinal relaxation rates, R_1, ^{15}N transverse relaxation rates, R_2, and {^{1}H}−^{15}N steady-state heteronuclear NOE values, at the ^{15}N frequency of 50.7 MHz, by analyzing proton-detected ^{1}H−^{15}N heteronuclear correlation spectra of ^{15}N-labeled HPt$_{ArcB}$. Reliable peak heights were obtained for 102 backbone amide resonances out of the expected 119. The peak heights for the other resonances could not be obtained owing to the spectral overlapping. R_1 and R_2 values were calculated by nonlinear least-squares fitting of monoexponential curves to the experimental data, and NOE values were calculated from the ratios of the peak heights in the spectra acquired with and without the ^{1}H saturation. For R_1, R_2, and NOE, 102, 92, and 99 relaxation parameters were reliably obtained, respectively (Figure 3). The 10% trimmed means and distributions were 1.73 ± 0.05 s^{-1} for R_1 and 10.38 ± 0.60 s^{-1} for R_2. The steady-state heteronuclear NOE values were uniformly high throughout the sequence except for in the N-terminal and C-terminal regions. The mean and distribution of the NOEs for this nonterminal region (Leu664−Ala775) was 0.73 ± 0.06. Generally, small NOE values reflect the presence of a picosecond to nanosecond time scale motion. The negative NOE values for the N-terminal four residues indicate the presence of significant flexibility in this region, and this feature is consistent with the finding that the conformation in this region diverged owing to a lack of long-range distance constraints. The overall rotational correlation time, τ_m, estimated from the mean and uncertainty (6.00 ± 0.33) of the 65 R_2/R_1 ratios that were limited to within 1 SD was 8.60 ± 0.31 ns. This value is comparable to those determined for other globular proteins with similar molecular weights.

Backbone Dynamics. The model-free approach developed by Lipari and Szabo (*27*) provides information on the overall and internal mobilities of a molecule. The ^{15}N R_1, R_2, and NOE data were first fitted to dynamic models (M1−5) under the assumption of isotropic rotational diffusion with the τ_m value fixed at 8.60 ns. Subsequently, one of the dynamic models was chosen for each amide ^{15}N spin according to the statistical selection protocol (*26*). The numbers of spins selected for the respective dynamic models were 31 (M1), 39 (M2), 1 (M3), 11 (M4), and 9 (M5). Of the total 92 resonances, no model was successfully fitted to the relaxation data of Trp746, which may undergo complicated motions on various time scales. Internal motion parameters (S^2, S_f^2, S_s^2, τ_{ef}, τ_{es}, and R_{ex}) as well as τ_m were simultaneously optimized finally using the dynamic model selected for each spin. As a result, τ_m was determined to be 8.63 ± 0.03 ns, which was almost the same as the value estimated initially from the limited R_2/R_1 ratios and used for the model selection (8.60 ns). The relaxation data for all the ^{15}N spins were simultaneously fitted well with the τ_m value of 8.63 ns to the respective dynamic models assigned initially. The reduced χ^2 for the overall fitting was 1.21, showing that the fitting was moderately good.

We also analyzed the relaxation data under the assumption of axially symmetric rotational diffusion. The R_2/R_1 ratios for the residues that may exhibit significant internal motions (Leu664, Leu670, Gly678, and Ile754) or conformational exchange (Gly716, Leu731, Gly735, and Trp761) were excluded according to the criteria described in Experimental Procedures (*28*). When an axially symmetric rotational diffusion tensor, D, is fit to the remaining 83 R_2/R_1 ratios and to the molecular coordinates of HPt$_{ArcB}$, the magnitude and orientation of D were initially estimated. The fitting result was better with the coordinates of the crystal structure of HPt$_{ArcB}$ (*9*) (reduced χ^2, 0.54) than with the coordinates of the solution structures (reduced χ^2, 1.05 ± 0.11). Thus, the coordinates of the crystal structure were used in the following model-free analysis with an anisotropic diffusion model. The numbers of spins selected for the respective dynamic models were 23 (M1), 15 (M2), 0 (M3), 25 (M4), and 29 (M5). The average correlation time derived from the finally optimized diffusion tensor ($1/2D_{\parallel} + 4D_{\perp}$) was 8.08 ± 0.02 ns, and the ratio of the principal values of the diffusion tensor ($D_{\parallel}/D_{\perp}$) was 1.37 ± 0.02, where $D_{\parallel}$ and $D_{\perp}$ are the longitudinal and transverse elements of the diffusion tensor, D, respectively. The orientation of the longitudinal axis of the diffusion tensor, which was determined on the model-free analysis, was close to that of the inertia moment tensor, which was estimated from the molecular coordinates (1.3° difference). The reduced χ^2 for the overall fitting was 0.97, showing that a slightly better fitting result was obtained

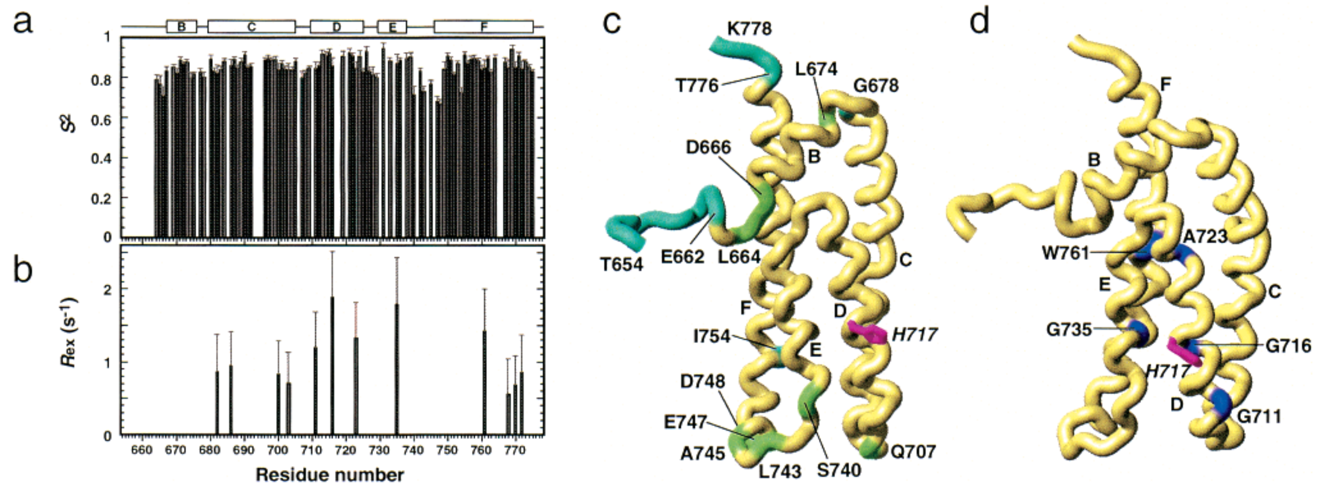

FIGURE 4: Internal motion parameters determined on model-free analysis with assumed isotropic rotational diffusion. Plots of order parameters, S^2 (a), and chemical exchange rates, R_{ex} (b), against residue numbers. The error bars indicate 1 SD values of the uncertainties estimated by means of Monte-Carlo simulations. The secondary structure is indicated at the top. (c) Mapping of the regions exhibiting internal motions on a picosecond to nanosecond time scale characterized by $\{^1H\}-^{15}N$ NOE values of <0.55 (cyan) or S^2 values of <0.8 (green). All the residues in the N-terminal (Thr654−Glu662) and C-terminal (Thr776−Lys778) regions are assumed to have small NOE values from the apparently descending curves of the NOEs at both ends of the sequence. (d) Mapping of the regions exhibiting very small conformational exchange on a microsecond to millisecond time scale characterized by R_{ex} values of >1.0 s^{-1} and <2.0 s^{-1} (blue). The side chain of the phosphorylation site, His717, is also shown in magenta. The secondary structure elements of the α-helices are labeled. The figures in (c) and (d) were drawn with the program MOLMOL (*22*).

under the assumption of axially symmetric rotational diffusion than under that of isotropic rotational diffusion.

The order parameters, S^2, determined with the isotropic and anisotropic models showed no statistically significant difference. Uniformly high order parameters, S^2 (0.86 ± 0.044), were obtained throughout the sequence except for the loop between helices E and F and the N-terminal 10 residues, for which S^2 could not be obtained (Figure 4a,c). Generally, a rigid part of a protein in terms of a picosecond to nanosecond time scale exhibits high S^2 values of about 0.85, and a flexible part exhibits low S^2 values of smaller than 0.8. The high S^2 as well as high NOE values obtained for HPt_{ArcB} indicate that the overall structure excluding both terminal ends is rigid on a picosecond to nanosecond time scale. The loop connecting helices E and F and the subsequent three residues of helix F (Ser740−Asp748) exhibited relatively low S^2 values of about 0.73 and effective correlation times for slow internal motions, τ_{es}, of about 1−3 ns, suggesting that this region undergoes motions on a nanosecond time scale.

R_{ex} values determined by model-free analysis indicate a region undergoing conformational exchange on a microsecond to millisecond time scale. The model-free analyses with the isotropic and anisotropic diffusion models revealed a slightly different feature of the R_{ex} values. For the isotropic model, R_{ex} values of larger than 1.0 s^{-1} were obtained for Gly711, Gly716, Ala723, Gly735, and Trp761, all of which are located spatially near the phosphorylation site, His717 (Figure 4b,d). In contrast, no residue exhibited a R_{ex} value larger than 1.0 s^{-1} for the axially symmetric rotational diffusion model.

A simple comparison between the reduced χ^2 values for overall fitting with the isotropic (1.21) and anisotropic (0.97) models seems to indicate that the anisotropic model is slightly better than the isotropic model for analysis of the relaxation data of HPt_{ArcB}. However, the dispersion of the ^{15}N R_2/R_1 ratios of HPt_{ArcB} was not large (1 SD, 8.4%) compared to the uncertainty of the data (5.3% on average). For more significant analysis under the assumption of anisotropic rotational diffusion, a wider dispersion of R_2/R_1 ratios with smaller uncertainties is required: for example, 1 SD of 20.4% for R_2/R_1 dispersion, which was observed with the same static magnetic field (50.7 MHz) for a nucleotide excision repair protein, XPA (*32*). Furthermore, the internal motion parameters, especially τ_{es} and R_{ex}, obtained on analysis with an anisotropic model are often affected by orientational deviation of the relevant amide NH bond vector from its accurate coordinates. For these reasons, it is difficult to judge which model is statistically more appropriate for analysis of the relaxation data of HPt_{ArcB}. However, it is clear from the obtained R_{ex} values that there seems to be no large motion on a slow time scale (microseconds to milliseconds) throughout the sequence except for the N-terminal 10 residues, for which R_{ex} could not be obtained. In addition, although there may be slow time scale motions in the vicinity of His717, they are very small.

Amide Hydrogen Exchange Rates and Protection Factors. The exchange of the amide protons of HPt_{ArcB} with solvent deuterons was monitored by recording successive HSQC spectra after dissolution of ^{15}N-labeled HPt_{ArcB}, which had been already lyophilized in H_2O, in ^2H_2O. The experiments were carried out at pH 5.5 and 6.5 so that the exponential decays caused by a wider range of exchange rates could be monitored. Of the 119 total backbone amide protons of HPt_{ArcB}, at least 78 and 72 exhibited exchange rates slow enough to be measured in the experiments at pH 5.5 and 6.5, respectively. The exchange rates for the other amide protons were too fast to be detected, except for those of Ala663 and Gln737, whose resonances overlapped in the HSQC spectra. The fitting of monoexponential curves to the experimental data was successful for 74 (pH 5.5) and 66 (pH 6.5) residues. Protection factors, P, were calculated for 50 amide hydrogens with larger exchange rates (>0.025 min^{-1} at pH 6.5) using the data obtained at pH 5.5 and for

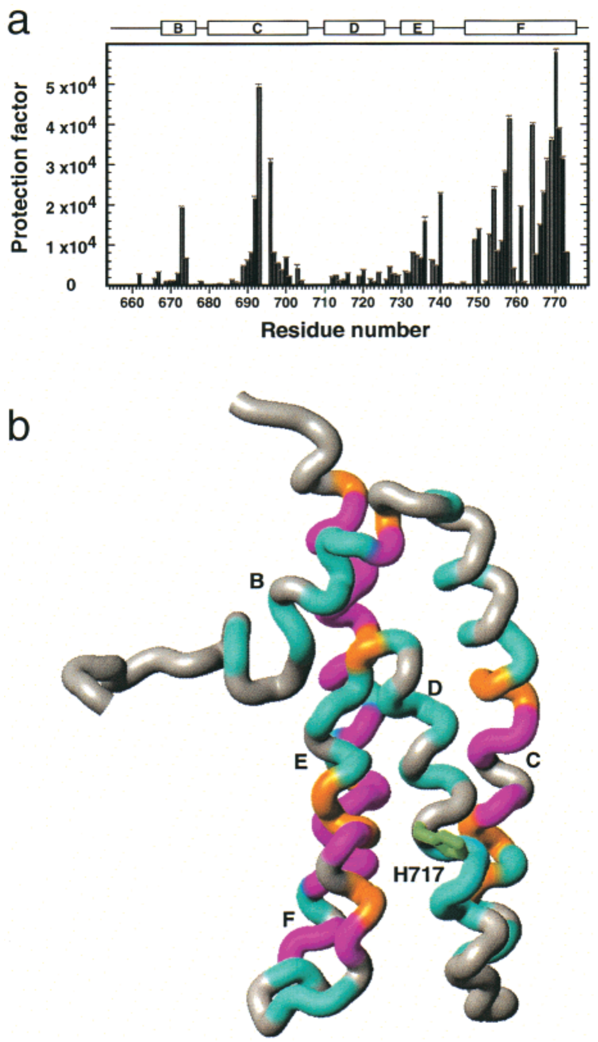

FIGURE 5: Protection factors estimated from amide hydrogen exchange rates. (a) A plot of protection factors, P, against residue numbers. The error bars indicate 1 SD values of the uncertainties estimated by means of Monte-Carlo simulations. The secondary structure is indicated at the top. (b) Mapping of the protection factors. The residues for which the amide hydrogen exchange rates were too fast to be detected in the proton/deuteron exchange experiments are drawn in gray. The residues with $P > 10$ and <4000 are drawn in light blue, >4000 and $<10\,000$ in orange, and $>10\,000$ in magenta. The side chain of the phosphorylation site, His717, is also shown in green. The secondary structure elements for the α-helices are labeled. The figure in (b) was drawn with the program MOLMOL (*22*).

28 with smaller exchange rates (<0.025 min^{-1} at pH 6.5) using the data obtained at pH 6.5, according to Bai et al. (Figure 5a). A protection factor represents the extent to which an amide hydrogen is protected from exchange with the solvent, thereby indicating the local stability around the amide hydrogen. The helix regions exhibited relatively high protection factors compared to the loop regions (Figure 5b). In particular, the central part of helix C and the whole of helix F were largely protected ($P \geq 10\,000$). In contrast, helix B, both ends of helix C, helix D, and helix E were less protected ($P < 10\,000$). The Gibbs free-energy for local transient unfolding of the helical regions was estimated for the amide protons for which the protection factors were available. The average values per residue were 4.92 (helix B), 4.96 (helix C), 4.64 (helix D), 5.31 (helix E), and 5.74 kcal/mol (helix F).

Interestingly, all the residues in helix D, which contains the phosphorylation site, His717, show relatively low protection factors of less than 4000 compared with those observed for the other helices (10000−60000) (Figure 5a). These low protection factors for helix D indicate that helix D may experience local transient unfolding on a millisecond to hour time scale more often than the other helices.

Effects of pH on the Histidine ^{1}H and ^{15}N Resonances. For characterization of the imidazole rings of all three histidine residues of HPt$_{\mathrm{ArcB}}$, His717, His730, and His763, 2D ^{1}H−^{15}N HMBC spectra were acquired with uniformly ^{15}N-labeled HPt$_{\mathrm{ArcB}}$ at various pHs between 3.69 and 9.41. The resonances of the imidazole protons attached to carbons, i.e., C^2−proton (H$^{\epsilon1}$) and C^4−proton (H$^{\delta2}$), were assigned by means of the correlations between H$^{\delta2}$ and C$^{\beta}$ nuclei in the 2D (HB)CB(CGCD)HD spectrum (*14*) and by means of the intraresidue NOEs between H$^{\delta2}$ and H$^{\epsilon1}$ nuclei in the 2D NOESY spectrum (Figure 6a, inset). In the 2D HMBC spectra obtained at pHs lower than 8.2, three cross-peaks corresponding to H$^{\epsilon1}$−N$^{\delta1}$, H$^{\delta2}$−N$^{\epsilon2}$, and H$^{\delta2}$−N$^{\delta1}$ were observed for each histidine residue. Most of the H$^{\epsilon1}$−N$^{\epsilon2}$ cross-peaks exhibited very weak intensities. The spectrum obtained at pH 6.87 is shown in Figure 6a as an example. In the spectra obtained at pHs higher than 8.4, cross-peaks derived from His763 were not observed, and those derived from His717 were broadened in the ^{15}N dimension, probably owing to exchange of the labile protons (H$^{\delta1}$ and H$^{\epsilon2}$) with the solvent. Figure 6b,c shows the pH titration curves for the N$^{\epsilon2}$, N$^{\delta1}$, H$^{\epsilon1}$, and H$^{\delta2}$ chemical shifts.

The pK_a values were estimated by fitting the Henderson−Hasselbalch equation to the pH titration data. The pK_a values estimated from the respective titration curves for H$^{\epsilon1}$, H$^{\delta2}$, N$^{\epsilon2}$, and N$^{\delta1}$ coincided with one another for His717 and His763, with average values of 6.76 and 7.09, respectively (Figure 6b,c). These values are close to the pK_a value of 6.9 for a solvent-exposed imidazole ring, which was found in a study on a model tripeptide, Gly-His-Gly (*33*). This agreement is consistent with the observation that these two imidazole rings are exposed to the solvent in the determined structure, the solvent accessibilities being 32.5%, 26.7%, and 11.0% for His717, His763, and His730, respectively (Figure 2b).

It has been reported that deprotonated and protonated imidazole ^{15}N nuclei usually resonate at about 250 and 170 ppm, respectively (*34*). However, both N$^{\epsilon2}$ and N$^{\delta1}$ nuclei of His717 at high pH resonate at about 205 ppm, which is almost the midpoint of these extreme resonances. Therefore, N$^{\epsilon2}$- and N$^{\delta1}$-deprotonated neutral tautomers, with an almost equal population of each tautomer, are likely to be exchanged at high pH rapidly compared to the difference between the two resonances (about 4 kHz). This result is different from that obtained for the phosphorylation site, His48, of chemotaxis-specific protein kinase CheA (*10*). The pH titration experiment involving the phosphotransfer domain of CheA showed that the N$^{\epsilon2}$-deprotonated tautomer is dominant for His48 (N$^{\epsilon2}$H/N$^{\delta1}$H tautomeric ratio, 3/7) at high pH with fast tautomerization; thus, the authors suggested that N$^{\delta1}$H is protected from deprotonation by a possible hydrogen bond involving N$^{\delta1}$H as the hydrogen donor. The crystal structure of HPt$_{\mathrm{ArcB}}$ suggests that Gln739 in helix E forms a hydrogen bond with the imidazole N$^{\delta1}$ atom of the phosphorylation site, His717, in helix D, such that the N$^{\epsilon2}$ site is exposed to

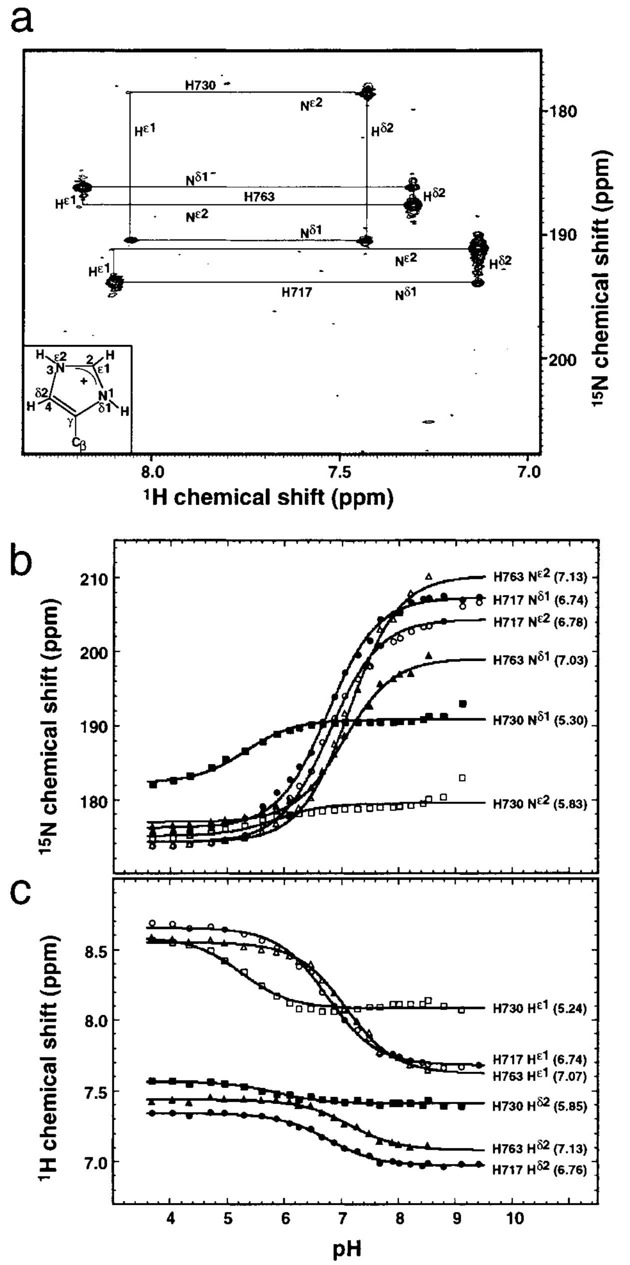

FIGURE 6: The pH titration of the histidine imidazole rings. (a) A portion of the 2D ^{1}H−^{15}N HMBC spectrum acquired with a DMX500 spectrometer with ^{15}N-labeled HPt$_{\mathrm{ArcB}}$ at pH 6.87 and 310 K. The cross-peaks correlate the resonances of $^{1}H^{\delta2}$ and $^{1}H^{\epsilon1}$ with those of $^{15}N^{\delta1}$ and $^{15}N^{\epsilon2}$ within a histidine imidazole ring. The connectivities in each imidazole ring are indicated by a quadrangle. The chemical structure of an imidazole ring in the protonated and positively charged form, which is usually assumed at acidic pH, is shown in the lower left corner. At high pH, either $N^{\epsilon2}$ or $N^{\delta1}$ is deprotonated and a neutral $N^{\delta1}$H- or $N^{\epsilon2}$H-tautomer is formed, respectively. The chemical shifts of the imidazole $^{15}N^{\delta1}$, $^{15}N^{\epsilon2}$ (b), $^{1}H^{\delta2}$, and $^{1}H^{\epsilon1}$ (c) nuclei of His717, His730, and His763 are shown as a function of pH. The curves represent the Henderson−Hasselbalch equations that fit best to the data. The apparent pK_a values estimated by nonlinear least-squares fitting are shown in parentheses.

the solvent (*8*, *9*). A similar hydrogen bond has also been proposed for the crystal structure of yeast Ypd1p, which is structurally similar to HPt$_{\mathrm{ArcB}}$ between the corresponding atoms, i.e., $O^{\epsilon1}$ of Gln86 and $N^{\delta1}$ of His64 (*6*, *7*). However, the pH titration results for HPt$_{\mathrm{ArcB}}$ showed that neither tautomer of His717 is dominant in HPt$_{\mathrm{ArcB}}$ in the solution state. Furthermore, this result is consistent with the report that mutant Q739A of HPt$_{\mathrm{ArcB}}$, in which glutamine at residue 739 is replaced with alanine, exhibits the same activity as the wild type (*35*), indicating that a hydrogen bond between His717 and Gln739 does not exist or, even if one exists, it is too weak to generate an unequal tautomeric ratio.

DISCUSSION

Possible Small Conformational Change Upon Phosphorylation. Recently, NMR ^{15}N relaxation and mutagenesis studies on the inactive form of a *Bacillus subtilis* response regulator, Spo0F, showed that the region surrounding the phosphorylation site, Asp54, has significant R_{ex} values (5−30 s^{-1}), which are indicative of motions on a microsecond to millisecond time scale (*36*). It was also shown that the locations of these residues with the slow time scale motions correlate with the surfaces for the interactions with other proteins involved in signal transduction, such as KinA (kinase), RapB (phosphatase), and Spo0B (phosphotransferase). The authors have concluded that regions with large R_{ex} values are associated with conformational changes upon phosphorylation (*36*). Examples of actual conformational changes upon phosphorylation of the active site aspartate residues in response regulator proteins have been reported for the chemotaxis protein CheY (*37*, *38*), the nitrogen-fixation regulatory protein FixJ (*39*), the sporulation regulatory protein Spo0A (*40*), and the nitrogen regulatory protein NtrC (*41*). In particular, for NtrC, phosphorylation induces large conformational changes around the active site, including displacement of β-strands and α-helices, and induces a register shift and axial rotation of a helix (*41*).

The α-helical regions of HPt$_{\mathrm{ArcB}}$ are rigid on both picosecond to nanosecond and microsecond to millisecond time scales on the basis of high S^2, high NOE, and no or very small R_{ex} values. In contrast, there is inhomogeneity as to much slower time scale motions. The protection factors of HPt$_{\mathrm{ArcB}}$, which were determined from the amide hydrogen exchange rates, show the presence of fluctuations (breathing motions) on a slower time scale (millisecond to hour) in helix D, which contains the phosphorylation site, His717 (Figure 5b). The very small R_{ex} values of between 1.0 and 2.0 s^{-1} in the vicinity of His717, which were obtained on the model-free analysis under the assumption of isotropic rotational diffusion (Figure 4d), might represent an influence of the fluctuations inferred from the low protection factors in helix D.

In analogy with Spo0F, which exhibits slow motions in the region surrounding the phosphorylation site, the slow time scale fluctuations in helix D of HPt$_{\mathrm{ArcB}}$ may imply that a conformational change occurs in helix D upon phosphorylation of His717. However, HPt$_{\mathrm{ArcB}}$ exhibits no or much smaller R_{ex} values in the vicinity of His717 compared with the R_{ex} values observed for Spo0F. Therefore, a possible conformational change in HPt$_{\mathrm{ArcB}}$ induced by phosphorylation of His717 is likely to be much smaller than the conformational changes in response regulators such as Spo0F and NtrC (*41*). In a study on the phosphotransfer domain of histidine kinase CheA, it was found that the backbone dynamics in the region around the phosphorylation site, His48, were rigid and that only small perturbations of the amide chemical shifts were observed in this region upon phosphorylation (*10*). The authors, therefore, suggested that a possible conformational change upon phosphorylation of His48 is localized and small (*10*). A possible conformational change in helix D of HPt_{ArcB} upon phosphorylation may be as small as that of the phosphotransfer domain of CheA. Since the well-determined crystal structure of helices D and E and the loop between them in HPt_{ArcB} (*9*) well matches the crystal structure of the corresponding regions of yeast Ypd1p (rms deviation for C^{α} atoms, 0.298 Å) (*6*), Ypd1p is expected to exhibit a similar dynamic character to HPt_{ArcB} and CheA.

The pH titration experiment showed that the imidazole ring of the phosphorylation site, His717, has a similar pK_a value to that of a solvent-exposed histidine imidazole ring. The determined solution structure of HPt_{ArcB} also demonstrated that the imidazole ring of His717 is exposed to the solvent. This supports the assumption that a large conformational change would not be required for His717 to receive a phosphoryl group from Asp576 in the intramolecular receiver domain and to donate it subsequently to Asp54 in the response regulator, ArcA, because these histidine and aspartate residues involved in phosphotransfer could easily come into contact with each other in the absence of a large conformational change of HPt_{ArcB}. Response regulators FixJ (*39*) and NtrC (*41*) undergo significant conformational changes upon phosphorylation. Especially in FixJ, backbone motions of up to 6 Å have been observed (*39*). On the contrary, the phosphotransfer domains of CheA (*10*) and ArcB are likely to undergo only small conformational changes upon phosphorylation. Considering these available examples, the localized and minor conformational changes in HPt domains upon phosphorylation in contrast to the large conformational changes in response regulators may be a common feature of His-to-Asp phosphorelay signal transduction because both HPt domains and response regulators exhibit respective similarities in their three-dimensional structures. Although the possible conformational change around the phosphorylation site of HPt_{ArcB} is probably small, it might facilitate fitting to the different binding partners including the intramolecular receiver domain and the response regulators when HPt_{ArcB} serves as a mediator in the multiple His-to-Asp phosphorelay system (*1*).

NMR analyses of the phosphorylated form of HPt_{ArcB} could make it possible to discuss straightforwardly the presumed structural difference between the phosphorylated and unphosphorylated proteins. Owing to the following reasons, unfortunately, structural analyses of the phosphorylated form of HPt_{ArcB} are not easy at present. A small amount of HPt_{ArcB} has been shown to be phosphorylated in vitro by incubating the protein with purified cytoplasmic membrane containing intact ArcB in the presence of ATP (*42*). However, the preparation of a large amount of the phosphorylated protein sufficient for NMR study, according to this procedure, would be difficult. In addition, a procedure for separation of phosphorylated HPt_{ArcB} from unphosphorylated HPt_{ArcB} has not been established yet to the best of our knowledge. Furthermore, the lifetime of the phosphorylated state in the membrane mixture for phosphorylation is estimated to be as short as about 30 min (*42*). Hence, analyses of the phosphorylated form of HPt_{ArcB} must await further experiments.

Protection Factors. HPt_{ArcB} exhibits protection factors of a 10^4 order of magnitude on average, with a maximum of 5.8×10^4 at the center of helix F (Figure 5). In contrast, higher protection factors of a 10^7 order have been reported for BPTI (*43*), thioredoxin (*44*), and calbindin D9k (*45*). The highest protection factor for oxidized equine cytochrome *c* is as high as 3×10^8 (*46*). Obviously, HPt_{ArcB} experiences transient local unfolding much more frequently than these proteins. On the other hand, the ribosomal protein L9, a 149 amino acid protein with an extremely elongated and flattened shape, exhibits lower protection factors of the order of 2×10^3 (*47*). Interestingly, *E. coli* chemotactic protein CheY (α/β parallel protein composed of 129 amino acids), which may interact with HPt_{ArcB} (*48*), has the same order of protection factors as HPt_{ArcB}, with a maximum of 6.0×10^4 (*49*). This similarity in the overall magnitude of the protection factors may imply that transient local unfolding of almost the same dynamic order is associated with the possible interaction between CheY and HPt_{ArcB}.

Unusual Character of His730. Both ^1H and ^{15}N chemical shift changes of His730 are confined to narrow ranges in a wide pH range compared to those of His717 and His763. Although the apparent pK_a values, which were estimated by fitting to the respective $H^{\delta 2}$, $H^{\epsilon 1}$, $N^{\epsilon 2}$, and $N^{\delta 1}$ titration curves of His730, diverge between 5.24 and 5.85, it is clear that the average pK_a value of 5.55 is significantly lower than that of a solvent-exposed histidine (~6.9) (Figure 6b,c). Similar titration curves were reported for the C^2−protons ($H^{\epsilon 1}$) of the histidine residues in human, horse, and sperm whale metmyoglobins (*50*). The curve for human metmyoglobin, for example, exhibited a total chemical shift change of 0.76 ppm, a downfield shift at high pH (resonance at 7.78 ppm), and a low pK_a value of 5.8 (*50*). The authors suggested that the low pK_a value is caused by a positively charged environment around the imidazole ring, perhaps due to nearby lysine residues. In HPt_{ArcB}, however, there is no lysine or arginine residue within 9 Å from His730. Instead, a metal ion, Zn^{2+}, was suggested to coordinate to His730, Glu756, Glu760, and symmetry-related Asp748 in the crystal structure of HPt_{ArcB} (*8*). Therefore, the low pK_a value of His730 may be due to the positive charge of the coordinating metal ion. Furthermore, the cross-peaks of His730 in HMBC spectra are sharp even at pHs up to 9.1 but broaden out at pH 9.4 to become undetectable, and its $N^{\epsilon 2}$ and $N^{\delta 1}$ chemical shifts are well separated at high pH. These results indicate that the exchange between the pair of deprotonated tautomers of His730 is suppressed at pHs below 9, probably because the imidazole ring is rather buried in the molecular surface (solvent accessibility, 11.0%) and is also involved in the metal ion coordination.

Although we performed HMBC and HSQC experiments with a sample containing 40 mM EDTA at pH 6.5 to determine whether the unusual pK_a value is due to the effect of a metal ion, no significant chemical shift change was observed in the spectra. Thus, the metal ion might coordinate strongly enough not to be detached from His730 by EDTA. We are continuing to investigate the unusual character of His730 and its biological implications.

CONCLUSION

In summary, the solution structure of the histidine-containing phosphotransfer domain of *E. coli* sensor kinase ArcB was determined by means of multidimensional NMR techniques using uniformly ^{15}N- or ^{15}N-,^{13}C-labeled samples. The structure contains five helices (B−F), of which helices C−F form a four-helix bundle, which is a common motif for HPt domains. In the crystal structure determined previously (*9*), an N-terminal region composed of five residues (Lys660−Leu664) was assigned to helix A, but in the solution structure, this region is too flexible to adopt a helical conformation. The backbone dynamics were also investigated by analyses of amide ^{15}N longitudinal and transverse relaxation rates and {^{1}H}−^{15}N heteronuclear NOE values under the assumption of isotropic or axially symmetric rotational diffusion. The obtained order parameters, S^2, as well as heteronuclear NOE values showed that the overall structure of HPt$_{\mathrm{ArcB}}$, except for both terminal ends and the loop connecting helices E and F, is rigid on a picosecond to nanosecond time scale. The small R_{ex} values obtained under the assumption of isotropic diffusion suggested that minor microsecond to millisecond time scale motions might occur in the vicinity of the phosphorylation site, His717. Slower time scale fluctuations in the backbone were studied as the rates of exchange of the amide protons with solvent deuterons. Uniformly low protection factors (<4000) in helix D, which contains His717, indicated that helix D undergoes a breathing motion involving local transient unfolding more frequently than the other helices. Taking these dynamic data and available examples of other HPt domains into consideration, we propose that HPt$_{\mathrm{ArcB}}$ undergoes a conformational change in helix D upon phosphorylation but that it is small and localized. Furthermore, the protonation states of histidine imidazole rings were characterized by means of pH titration experiments. The results showed that the pK_{a} value of the imidazole ring of His717 (6.76) is close to that of a solvent-exposed imidazole ring (∼6.9) and that the pair of deprotonated neutral tautomers are exchanged rapidly. This is consistent with the solution structure of HPt$_{\mathrm{ArcB}}$, in which the imidazole ring of His717 is exposed to the solvent. Since the HPt domains exhibit a structural similarity to one another (*51*), the characters of the internal dynamics and the phosphorylation site histidine, which are reported here for HPt$_{\mathrm{ArcB}}$, are expected to be common to other HPt domains as well.

ACKNOWLEDGMENT

The authors wish to thank Dr. Masato Kato and Dr. Toshio Hakoshima for the helpful discussions.

SUPPORTING INFORMATION AVAILABLE

Two tables containing the internal motion parameters of HPt$_{\mathrm{ArcB}}$ (S^2, $S_f^{\,2}$, τ_{e}, and R_{ex}) obtained by model-free analyses under the assumption of isotropic or anisotropic rotational diffusion and the results of the pH titration experiments for the histidine imidazole rings. This information is available free of charge via the Internet at http://pubs.acs.org.

REFERENCES

1. Mizuno, T. (1998) *J. Biochem. (Tokoyo) 123*, 555−563.
2. Hoch, J. A., and Silhavy, T. J. (1995) *Two-Component Signal Transduction*, American Society for Microbiology Press, Washington, DC.
3. Wurgler-Murphy, S. M., and Saito, H. (1997) *Trends Biochem. Sci. 22*, 172−176.
4. Matsushika, A., and Mizuno, T. (1998) *J. Biochem. (Tokoyo) 124*, 440−445.
5. Matsushika, A., and Mizuno, T. (2000) *J. Biochem. (Tokoyo) 127*, 855−860.
6. Xu, Q., and West, A. H. (1999) *J. Mol. Biol. 292*, 1039−1050.
7. Song, H. K., Lee, J. Y., Lee, M. G., Moon, J., Min, K., Yang, J. K., and Suh, S. W. (1999) *J. Mol. Biol. 293*, 753−761.
8. Kato, M., Mizuno, T., Shimizu, T., and Hakoshima, T. (1997) *Cell 88*, 717−723.
9. Kato, M., Mizuno, T., Shimizu, T., and Hakoshima, T. (1999) *Acta Crystallogr. D55*, 1842−1849.
10. Zhou, H., and Dahlquist, F. W. (1997) *Biochemistry 36*, 699−710.
11. Varughese, K. I., Madhusudan, Z. X. Z., Whiteley, J. M., and Hoch, J. A. (1998) *Mol. Cell 2*, 485−493.
12. McEvoy, M. M., Muhandiram, D. R., Kay, L. E., and Dahlquist, F. W. (1996) *Biochemistry 35*, 5633−5640.
13. Cavanagh, J., Fairbrother, W. J., Palmer, A. G., III, and Skelton, N. J. (1996) *Protein NMR Spectroscopy*, Academic Press, San Diego.
14. Yamazaki, T., Forman-Kay, J. D., and Kay, L. E. (1993) *J. Am. Chem. Soc. 115*, 11054−11055.
15. Hu, W., and Zuiderweg, E. R. P. (1996) *J. Magn. Reson. B113*, 70−75.
16. Marion, D., Ikura, M., Tschudin, R., and Bax, A. (1989) *J. Magn. Reson. 85*, 393−399.
17. Delaglio, F., Grzesiek, S., Vuister, G. W., Zhu, G., Pfeifer, J., and Bax, A. (1995) *J. Biomol. NMR 6*, 277−293.
18. Garrett, D. S., Powers, R., Gronenborn, A. M., and Clore, G. M. (1991) *J. Magn. Reson. 95*, 214−220.
19. Wüthrich, K. (1986) *NMR of Proteins and Nucleic Acids*, John Wiley & Sons, Inc., New York.
20. Güntert, P., Mumenthaler, C., and Wüthrich, K. (1997) *J. Mol. Biol. 273*, 283−298.
21. Brünger, A. T. (1993) *X-PLOR 3.1: A System for X-ray Crystallography and NMR*, Yale University Press, New Haven, CT.
22. Koradi, R., Billeter, M., and Wüthrich, K. (1996) *J. Mol. Graphics 14*, 51−55.
23. Laskowski, R. A., Rullmann, J. A. C., MacArthur, M. W., Kaptein, R., and Thornton, J. M. (1996) *J. Biomol. NMR 8*, 477−486.
24. Farrow, N. A., Muhandiram, R., Singer, A. U., Pascal, S. M., Kay, C. M., Gish, G., Shoelson, S. E., Pawson, T., Forman-Kay, J. D., and Kay, L. E. (1994) *Biochemistry 33*, 5984−6003.
25. Bevington, P. R., and Robinson, D. K. (1992) in *Data Reduction and Error Analysis for the Physical Sciences* 2nd ed., pp 38−52, 161−164, WCB/McGraw-Hill, New York.
26. Mandel, A. M., Akke, M, and Palmer, A. G., III. (1995) *J. Mol. Biol. 246*, 144−163.
27. Lipari, G., and Szabo, A. (1982) *J. Am. Chem. Soc. 104*, 4546−4570.
28. Tjandra, N., Feller, S. E., Pastor, R. W., and Bax, A. (1995) *J. Am. Chem. Soc. 117*, 12562−12566.
29. Bai, Y., Milne, J. S., Mayne, L., and Englander, S. W. (1993) *Proteins: Struct., Funct., Genet. 17*, 75−86.
30. Xia, B., Cheng, H., Skjeldahl, L., Coghlan, V. M., Vickery, L. E., and Markley, J. L. (1995) *Biochemistry 34*, 180−187.
31. Wishart, D. S., and Sykes, B. (1994) *Methods Enzymol. 239*, 363−392.
32. Ikegami, T., Kuraoka, I., Saijo, M., Kodo, N., Kyogoku, Y., Morikawa, K., Tanaka, K., and Shirakawa, M. (1999) *J. Biochem. (Tokoyo) 125*, 495−506.
33. Markley, J. L. (1975) *Acc. Chem. Res. 8*, 70−80.
34. Singer, A. U., and Forman-Kay, J. D. (1997) *Protein Sci. 6*, 1910−1919.
35. Matsushika, A., and Mizuno, T. (1998) *Biosci. Biotechnol. Biochem. 62*, 2236−2238.
36. Feher, V. A., and Cavanagh, J. (1999) *Nature 400*, 289−293.
37. Cho, H. S., Lee, S. Y., Yan, D., Pan, X., Parkinson, J. S., Kustu, S., Wemmer, D. E., and Pelton, J. G. (2000) *J. Mol. Biol. 297*, 543−551.

38. Halkides, C. J., McEvoy, M. M., Casper, E., Matsumura, P., Volz, K., and Dahlquist, F. W. (2000) *Biochemistry 39*, 5280−5286.
39. Birck, C., Mourey, L., Gouet, P., Fabry, B., Schumacher, J., Rousseau, P., Kahn, D., and Samama, J. P. (1999) *Structure 7*, 1505−1515.
40. Lewis, R. J., Brannigan, J. A., Muchova, K., Barak, I., and Wilkinson, A. J. (1999) *J. Mol. Biol. 294*, 9−15.
41. Kern, D., Volkman, B. F., Luginbuehl, P., Nohaile, M. J., Kustu, S., and Wemmer, D. E. (1999) *Nature 402*, 894−898.
42. Ishige, K., Nagasawa, S., Tokishita, S., and Mizuno, T. (1994) *EMBO J. 13*, 5195−5202.
43. Schulman, B. A., and Kim, P. S. (1994) *Protein Sci. 3*, 2226−2232.
44. Jeng, M. F., and Dyson, H. J. (1995) *Biochemistry 34*, 611−619.
45. Skelton, N. J., Kordel, J., Akke, M., and Chazin, W. J. (1992) *J. Mol. Biol. 227*, 1100−1117.
46. Milne, J. S., Mayne, L., Roder, H., Wand, A. J., and Englander, S. W. (1998) *Protein Sci. 7*, 739−745.
47. Lillemoen, J., Cameron, C. S., and Hoffman, D. W. (1997) *J. Mol. Biol. 268*, 482−493.
48. Kato, M., Shimizu, T., Mizuno, T., and Hakoshima, T. (1999) *Acta Crystallogr. D55*, 1257−1263.
49. Lacroix, E., Bruix, M., Lopez-Hernandez, E., Serrano, L., and Rico, M. (1997) *J. Mol. Biol. 271*, 472−487.
50. Hayes, M. B., Hagenmaier, H., and Cohen, J. S. (1975) *J. Biol. Chem. 250*, 7461−7472.
51. Robinson, V. L., Buckler, D. R., and Stock, A. M. (2000) *Nat. Struct. Biol. 7*, 626−633.
52. Kraulis, P. J. (1991) *J. Appl. Crystallogr. 24*, 946−950.
53. Merritt, E. A., and Bacon, D. J. (1997) *Methods Enzymol. 277*, 505−524.

BI001619G